research papers

Implementation of a combined SAXS/WAXS/QEXAFS set-up for time-resolved *in situ* experiments

**Sergey Nikitenko,[a] Andrew M. Beale,[b] Ad M. J. van der Eerden,[b]
Simon D. M. Jacques,[c] Olivier Leynaud,[c] Matthew G. O'Brien,[b]
Dirk Detollenaere,[d] Reinier Kaptein,[e] Bert M. Weckhuysen[b] and Wim Bras[f]***

[a]KU Leuven, DUBBLE CRG/ESRF, F-38043 Grenoble, France, [b]Inorganic Chemistry and Catalysis,
Debye Institute for NanoMaterials Science, Utrecht University, Sorbonnelaan 16, 3584 CA, Utrecht,
The Netherlands, [c]Industrial Materials Group, Christopher Ingold Laboratories, Department of
Chemistry, University College London, London WC1H 0AJ, UK, [d]University of Gent DUBBLE@-
ESRF, F-38043 Grenoble, France, [e]University of Groningen Physics Department, Nijenborgh 4,
9747 AG Groningen, The Netherlands, and [f]Netherlands Organization for Scientific Research
(NWO), DUBBLE@ESRF, F-38043 Grenoble, France. E-mail: wim.bras@esrf.fr

It has previously been shown that there are many benefits to be obtained in combining several techniques in one *in situ* set-up to study chemical processes in action. Many of these combined set-ups make use of two techniques, but in some cases it is possible and useful to combine even more. A set-up has recently been developed that combines three X-ray-based techniques, small- and wide-angle X-ray scattering (SAXS/WAXS) and quick-scanning EXAFS (QEXAFS), for the study of dynamical chemical processes. The set-up is able to probe the same part of the sample during the synthesis process and is thus able to follow changes at the nanometre to micrometre scale during, for example, materials self-assembly, with a time resolution of the order of a few minutes. The practicality of this kind of experiment has been illustrated by studying zeotype crystallization processes and revealed important new insights into the interplay of the various stages of ZnAPO-34 formation. The flexibility of this set-up for studying other processes and for incorporating other additional non-X-ray-based experimental techniques has also been explored and demonstrated for studying the stability/activity of iron molybdate catalysts for the anaerobic decomposition of methanol.

Keywords: XAFS; SAXS; WAXS.

1. Introduction

There are distinct advantages to be found in combining several independent analytical techniques to study chemical processes as they occur. This is well illustrated in situations where either the time resolution is so high that the results of independent experiments are difficult to synchronize or in cases where the sample environment is complicated and the experiments might be difficult to reproduce exactly. In addition, simultaneously performed experiments often enable a more detailed understanding of the temporal behaviour and interplay of, for instance, chemical species present during solid formation, catalytic reactions *etc.* If one is therefore interested in a sequence of events such as phase transitions, changes in local chemical environments, crystallization *etc.*, the simultaneous acquisition of data from

combined multiple techniques can be rather useful and in some cases crucial.

In synchrotron radiation research the above principles have been implemented by, for instance, using X-ray absorption spectroscopy (XAFS) and diffraction (Sankar *et al.*, 1993) or the combination of small- and wide-angle X-ray scattering (SAXS and WAXS) (Bark *et al.*, 1992; Bras *et al.*, 1993). Obviously this principle can be extended to the combination of synchrotron radiation techniques with non-X-ray-based techniques such as differential scattering calorimetry (DSC) and SAXS/WAXS (Bras, Derbyshire, Devine *et al.*, 1995), light scattering/SAXS/WAXS (Zachmann & Wutz, 1993), Raman scattering/SAXS/WAXS (Bryant *et al.*, 1998), SAXS/FTIR (Fourier transform infrared spectroscopy) (Bras, Derbyshire, Bogg *et al.*, 1995), XAFS/FTIR (Newton *et al.*, 2004), UV–Vis/Raman/XAFS for both gas and liquid phase heterogeneous

catalysis (Beale *et al.*, 2005; Briois *et al.*, 2005) *etc* (Bras & Ryan, 1998).

The choice of when it is sensible to use a combination of simultaneous techniques is something that has to be carefully weighed up since in most cases this approach results in the loss of some data quality in at least one of the techniques. There has to be a serious advantage in collecting the data simultaneously instead of utilizing optimized independent techniques. An example of the loss of data quality is, for instance, in the over- and under-focus of the X-ray beam in a combined SAXS/WAXS experiment in the SAXS and WAXS detectors, respectively. Also, the combination of, for instance, DSC with EXAFS suffers from this since the requirement that the sample should be accessible by X-rays is contradictory to the requirement that the thermal environment of the sample should be completely isolated. Notwithstanding these limitations, there are cases where the synergy between the techniques is obvious and which go beyond the simple circumvention of the need to repeat identical experimental conditions for separate measurements, which is, although seemingly a trivial point, far from easy to achieve experimentally.

The wish to be able to follow crystallization and chemical processes from the very early stage (where the structures have not yet developed into sizes that can be studied with diffraction and scattering techniques) to the later stage where crystalline morphologies have formed and the subsequent growth process could be characterized with respect to growth kinetics have influenced the design of the XAFS beamline placed in BM26A at the ESRF. We have developed equipment that makes use of the QEXAFS (quick-scanning EXAFS) technique (Frahm, 1989, 1988) and have combined this with both SAXS as well as WAXS. The equipment is designed to be able to follow processes for which a time resolution of approximately 10 frames min^{-1} is sufficient. If one wants to study faster processes with spectroscopic techniques, this equipment is not suitable and one should use either fast sequential energy-scanning QEXAFS monochromators (Frahm *et al.*, 2004) or energy-dispersive techniques, even though this means that, for the latter, the samples are exposed to a rather high temporal X-ray dose and might suffer from radiation damage or, for instance, chemical reactions might be influenced by the X-rays (Mesu *et al.*, 2005).

In order to completely describe the whole process it will be clear that one has to start from a well characterized sample and that the final product again should be well characterized, maybe not only with the techniques used in the experiment but also by additional techniques that can render extra information such as microscopy (scanning and transmission electron microscopy *etc.*). There are numerous research fields where the application of the above-mentioned techniques could be rather useful. For instance, in glass ceramics (Bras, 1998; Bras *et al.*, 2005), porous materials like heteroatom-substituted aluminophosphates (MeAPO) (Sankar *et al.*, 1995), cement setting (Scheidegger *et al.*, 2000, 2001) and bone mineralization (Savarino *et al.*, 1998) are just some of the examples for which the experimental techniques that are combined in our set-up can render useful information.

As an example of the usefulness of the applied method we show data on the crystallization of CoAPO. This system was studied previously by *in situ* diffuse reflectance spectroscopy and electron spin resonance (Weckhuysen *et al.*, 2000), and more recently by independent *in situ* XAFS and SAXS/WAXS techniques (Grandjean *et al.*, 2005), but since these results were not obtained during one combined measurement it was difficult to understand exactly how changes in each technique corresponded to each other, so the finer details of the crystallization process could not be understood.

2. Beamline and experimental set-up

The experiments were carried out on the Dutch Belgian beamline BM26A at the ESRF (Borsboom *et al.*, 1998). The optical layout of the beamline is represented in Fig. 1. The radiation source is the 0.4 T ESRF bending magnet. The beamline receives 2 mrad of the radiation fan. The optics set-up contains two mirrors: an (optional) upward-cooled collimation mirror (1200 × 150 × 50 mm) with horizontal surface grooves filled with a GaIn alloy on the surface parallel to the X-ray beam, and a second focusing mirror which has the same dimensions and specifications as the first although there are no cooling grooves on the surface. For the collimation mirror a cooling blade can be inserted into the grooves so that side-cooling is achieved without unnecessary mechanical constraint, which could affect the required bending accuracy. The mirror has, besides the bare Si surface, a Pt-coated strip along the length of the mirror. Depending on the energy, a
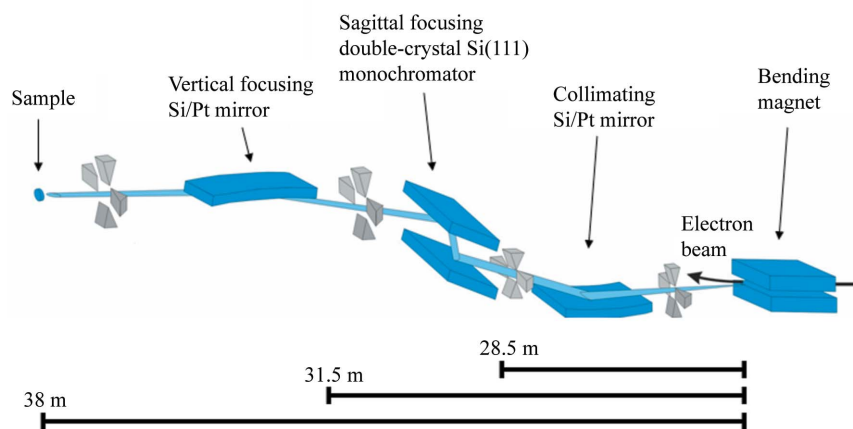

Figure 1
Optical layout of the BM26A beamline at ESRF. The optical elements are an (optional) collimating mirror, a double-crystal sagittal focusing monochromator and a vertically focusing mirror. Both mirrors have a strip with a bare silicon surface as well as a strip with a Pt coating. Depending on the energy range and the requirement for higher harmonic rejection, one of the strips can be brought into the beam by a sideways translation.

sideways translation can bring into the beam the appropriate surface for higher harmonic rejection without needing to change the mirror inclination. The determined factor of the higher harmonic suppression is better than 10^5 using two mirrors. The surface roughness is 1.5 Å (r.m.s.) and the slope error is less than 1.5 µrad over the whole surface. A Si(111) monochromator was used for these experiments which has the option of sagittal focusing, although for time-resolved measurements this was not employed owing to the length of time taken to bend the second crystal with respect to the time resolution needed to perform QEXAFS measurements. The second, focusing, mirror has the same dimensions and specifications as the collimating mirror, apart from the cooling grooves on the surface.

The layout of the experimental hutch for combined SAXS/WAXS/EXAFS experiments is shown in Fig. 2. For the spectroscopy experiments we have the choice between a transmission and a fluorescence configuration. The ionization chambers used in the transmission geometry are low-noise Oxford (Oxford-Danfysik) chambers designed specially for XAS measurements and are read out by low-noise current preamplifiers (manufactured by NOVELEC SA) having voltage/frequency converters (operating from 0 to 1 MHz) on the output connected to the scaler. The amplifiers have a dynamical range for the input current from 0.1 mA to 10 nA with six decades of magnitude. For fluorescence experiments we utilize a nine-element monolithic Ge fluorescence detector with digital XPRESS-XRay signal-processing electronics (Derbyshire et al., 1999; Farrow et al., 1995).

The addition of SAXS to the already existing combined XAFS/diffraction set-up is somewhat complicated since a long kapton-windowed (two windows both 40 µm thick) vacuum chamber has to be inserted between the sample and the SAXS detector. However, the transmitted intensity also has to be measured to a high accuracy and the presence of the SAXS flight tube and the requirement to preserve the SAXS data quality prevents the use of a conventionally used ion chamber. Still, an ion chamber can be used by mounting it on a translation stage parallel to a He-filled flight tube and driving it into position when the spectroscopy data is collected. Unfortunately this adds several moving components to the system. The alternative is to mount an accurate photodiode on the position of the SAXS beam stop. The latter option is only possible with a somewhat larger beam stop and a very stable beam.

All the data discussed in this work have been obtained by using a photodiode ODD-15W ($\sim$15 mm^2 active area) from Opto Diode.

The SAXS/WAXS data were recorded simultaneously using a combination of two detectors. For the SAXS data a gas-filled quadrant detector positioned at a distance of 1.8 m from the sample was used. This detector has the advantage of a larger active area that a two dimensional detector offers, but avoids the requirement of post-processing the data via a radial integration (Gabriel & Dauvergne, 1982).

For the WAXS data a position-sensitive curved gaseous INEL CPS 590 detector was used (Bras et al., 1993). Both these detectors are intrinsically count-rate limited. However,
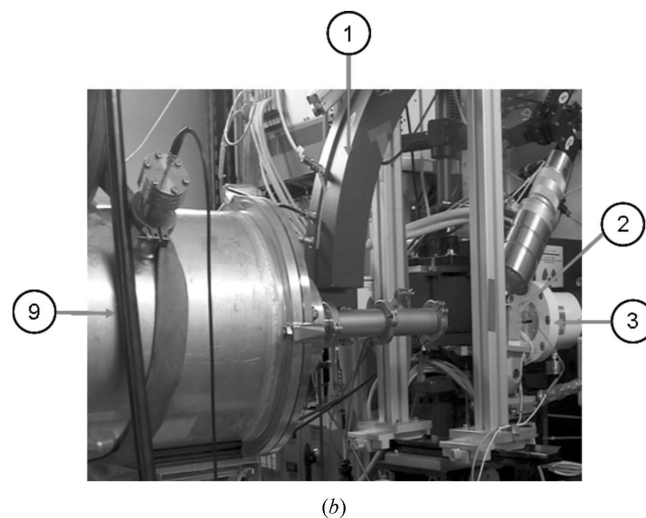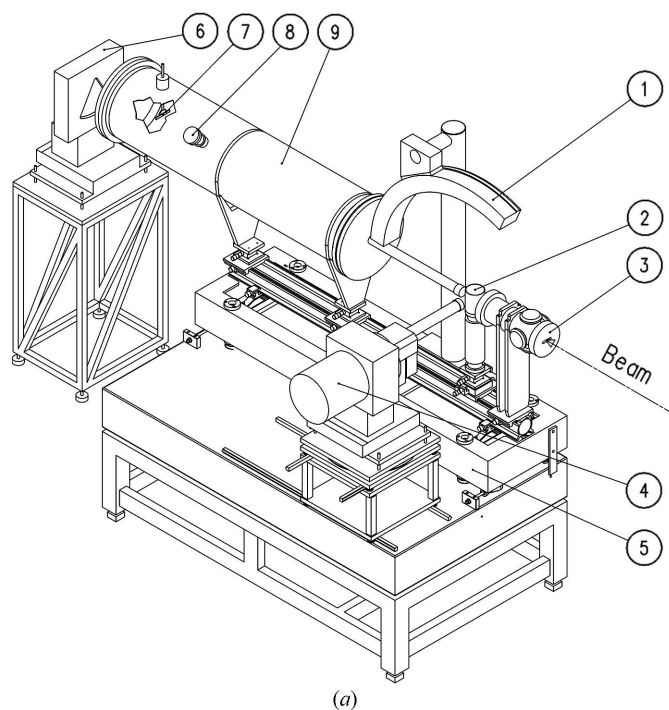

(a)

(b)

Figure 2
Combined SAXS/WAXS/XAFS experimental set-up (a) and accompanying photograph (b). The small vacuum tube between the main flight tube to the SAXS detector and the sample can be replaced by a translation stage with both an ionization chamber and He-filled tube which can alternately be put into the X-ray path. 6: quadrant gas-type SAXS detector; 7: the photodiode as a second XAFS detector mounted in front of the beam stop (I_t); 8: feedthrough flange for the photodiode input/output; 9: evacuated or He-filled tube.

this does not pose a problem with the time resolution that can be achieved with this method/set-up since the largest part of the duty cycle is taken up by the scanning of the monochromator which is mechanically limited (with a maximum scanning speed of 1° s^{-1}). In a data collection period of 2–4 s acceptable scattering data can be obtained.

The time-resolved experiments were performed in the QEXAFS mode in which the monochromator is scanned rapidly (non-stop) around a specific absorption edge
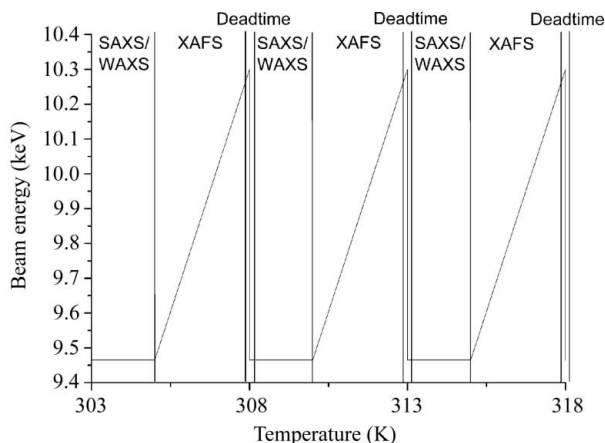
Figure 3
Time frame diagram for combined SAXS/WAXS/XAFS data collection. The scattering/diffraction data are collected during a brief period where the monochromator position is fixed. A QEXAFS scan is started subsequently. After this scan the monochromator is rotated back to the position/energy where the scattering data are collected.

(minimum entire spectrum collection time of ~ 60 s and a typical energy resolution of ~ 1.7 eV point^{-1}) in combination with (quasi-)simultaneous WAXS and SAXS data collection at a fixed energy (typical data collection time ~ 20 s frame^{-1}). In Fig. 3 we show the time–photon-energy profile that we have used in these experiments. As can be seen from the figure, the X-ray diffraction/scattering data is acquired while the monochromator is kept in a fixed position from a minimum of 2 s (depending on the required sampling data statistics) before a subsequent energy scan is started, during which the XAFS data are collected.

Depending on the required energy scan range this can last from 10 to 60 s, though the photon flux on the sample is sufficient to achieve even higher time resolutions. After the XAFS scan is complete, the monochromator is rotated back to the starting energy and the whole process is started again. In principle, this method is straightforward; however, complications can arise owing to the fact that one prefers to acquire the scattering data at energies between 8 and 15 keV while the X-ray absorption edge of interest falls outside this range. The reason for the preferred energy range for scattering data collection is that the extent of the parasitic scattering cone is photon-energy-independent, but the scattering pattern becomes rather compressed with regard to scattering vector range at higher photon energies. In this case the low angle resolution, and therefore the advantage of performing this technique combination, is lost.

In theory one could also collect scattering data during the energy scan, making use of the rapid change in X-ray scattering cross section to perform anomalous SAXS and WAXS measurements. Thus far we have not attempted this seriously since the issues regarding detector calibrations and the data quality are not simple to solve.

The data acquisition software was developed at the SRS Daresbury Laboratory and adapted to be able to control the motor and detector systems of the BM26A beamline. Depending on the design of the sample cell, it is feasible to also collect data using non-X-ray-based techniques; in the case where optical methods are employed, the implementation is fairly straightforward.

The advantage of using energy-dispersive schemes is a better time-resolution up to the millisecond scale, but the disadvantage is a high risk of the beam influence on the processes in the sample because of extremely high photon density in the beam spot. For example, the polychromatic photon density at an energy-dispersive beamline at ESRF is $\sim 10^{12}$ photons s^{-1} in a 20 µm beam spot and there are some indications that the beam actually induces damage to the liquid samples we have used in our measurements (Mesu *et al.*, 2005). In a comparison of the XAFS data obtained with an energy-dispersive beamline we found indications that the X-ray beam influences the reaction mixture in the cuvette whereas some previous measurements on BM26A using a standard scanning set-up with the same samples demonstrate that the radiation damage was negligible. Also, the complication would arise that from the pink beam we would obtain a quasi-Laue pattern while the SAXS data would have to be de-smeared. These problems do not inhibit all experiments, but if not required on the basis of time-resolution it is evident that one is better off using the QEXAFS scheme.

In our set-up we used a beam spot of ~ 0.5 mm $\times$ 0.5 mm and the photon flux was $\sim 10^9$ photons s^{-1}; then the photon density was less by a factor 10^5–10^6 in comparison with the energy-dispersive set-up at ESRF.

2.1. Experimental conditions

Illustrating the possibilities and the usefulness of the combined approach, we discuss here the results obtained from two different types of experiment: a study of the crystallization of a microporous Zn^{2+}-doped aluminium phosphate and an iron molybdate catalyst during anaerobic decomposition of methanol. In a typical synthesis of ZnAPO with ~ 2.5 wt% Zn, the following chemicals were used: 0.131 g $Zn(NO_3)_3.4H_2O$ (Acros Organics 99%), 69 ml H_3PO_4 (Acros Organics 85 wt% in water), 1.04 ml triethylamine (Acros Organics 99%) and 0.658 g pseudobohemite alumina CATAPAL B 73.6 wt% Al_2O_3 (Sasol North America Inc.). The white amorphous precursor gel used in the experiments possessed the stoichiometry $Zn_xAl_{1-x}PO_4$ where $x = 0.05$ (zinc content ~ 2.5 wt%) and a pH of ~ 3.5 (Christensen *et al.*, 1998). The preparation of an iron molybdate catalyst is described elsewhere (Beale *et al.*, 2008). Since such processes normally take place over a number of hours, the time resolution was accordingly adapted to the process and set to 5 min frame^{-1}. Thus a total cycle time of 5 min was employed for both sets of experiments to collect this data (3 min for XAS and 2 min for SAXS/WAXS which includes a 10 s dead-time to move the monochromator back to the start position and a further 10 s to move the I_t photodiode into/out of the beam). The *in situ* zeotype formation study was performed using a hydrothermal reactor cell which allows for the measurement of X-ray data in transmission mode. XAFS data were recorded at the Zn *K*-edge (9.66 keV), while the corresponding SAXS/WAXS data

were collected below this energy at 9.465 keV (1.3098 Å) during temperature ramping at 1 K min^{-1} to a temperature of 448 K. Using this set-up, analysable EXAFS data were obtainable up to 12 Å, along with WAXS data over a 2θ range of 45° using the INEL detector (although 'useable data' extended from 12 to 27° owing to the need to avoid the contaminant Bragg peaks from the mica windows) whereas the SAXS data covered a q-range $0.3 < q < 2$ nm^{-1}.

In the catalytic study the potential of a novel one-dimensional iron molybdate type catalyst [Mo:Fe (3:1)] normally used for the production of formaldehyde (Soares & Portela, 2005) was studied during temperature ramping to 523 K in a methanol/helium flow using a classical heated capillary as a simulation of a packed bed reactor (Clausen *et al.*, 1991). A 0.7 mm-diameter quartz capillary was used to contain the sample (sieved to 30–40 mesh size) whilst MeOH/He mix was supplied to the sample using a bubbler (based on the vapour pressure of methanol at 294 K the methanol saturation in the gas stream was estimated to be ~15%) whilst air grade zero was used in an attempt to perform oxidative regeneration. The rate of both gases was controlled using mass flow devices, triggered by 5 V TTL pulses from outside the experimental hutch. Online product analysis was also performed using a European Spectrometry Systems ecoSys-P Man-Portable mass spectrometer with a capillary inlet and heated inlet tube in order to understand further possible structure/function relationships. XAFS studies were performed at the Mo K-edge (20000 eV) whilst SAXS/WAXS measurements were performed below the Mo K-edge at 17658.98 eV (λ = 0.702104 Å).

3. Results

3.1. *In situ* study of microporous aluminophosphate crystallization

Previously it has been shown through the use of both scattering and spectroscopic techniques that the formation process of pure and metal-substituted (Co)AlPOs can be described as a three-step process, consisting of an initial reaction between the reactants to form a gel followed by gradual aggregation and then crystallization (Scheidegger *et al.*, 2000). The salient points from this previous work were (i) the formation of initial aggregates of size ~8 nm which already contained a majority of tetrahedral Al^{3+}/P^{5+} species (as observed by XAFS and Raman spectroscopy); (ii) heating of these gels (from 303–433 K) caused the aggregates to grow until a size of ~40 nm was reached before crystallization (as determined by the emergence of Bragg peaks seen in both the SAXS and WAXS detectors) of the final microporous aluminophosphate phase began at temperatures of ~433 K; (iii) transition metals such as Co^{2+} changed their coordination state from octahedral to tetrahedral during the aggregation (slowly) and crystallization steps (fast); (iv) the last measurable aggregates observed by SAXS possessed a similar size to that of the first crystallites as determined from peak profiling; (v) analysis of the growth of the peaks revealed that the

mechanisms of crystallization were similar and indicated that the materials crystallized *via* either (i) a one-dimensional growth with a constant nucleation rate or (ii) a one-dimensional growth phase-boundary-controlled crystallization process (Hulbert, 1969). Despite the amount of detailed insight gleaned from such a multiple technique approach there remained questions regarding the interplay between the steps and how this leads to the formation of the final crystalline sample.

The XAFS and WAXS data indicated that the initial synthesis gel contains predominantly tetrahedral Zn^{2+} (XAFS edge position ~9.666 keV) and appears diffraction amorphous. This behaviour contrasted with that of Co^{2+} and suggested that the initial Zn^{2+} species formed interactions with the Al–O–P species before heating began. The SAXS scattering profile did not appear to contain any marked features, which could be associated with the presence of clear primary units. However, the intensity $I(q)$ closely follows a power-law decay q^{-n} (where $n \simeq 2$), which is slower than the asymptotic behaviour of $I(q)$ with $n \simeq 4$ predicted by the Porod law for compact particles with sharp interfaces, indicating that this system was more complex. However, by focusing on the q range from 0.025 to 0.1 nm^{-1} and after removing the leading q^{-2} decay, the $I(q) \times q^2$ dependence, the plots exhibit a broad maximum (q max) which can be fitted with a Gaussian function and approximated to the inverse of the typical size of possible gel aggregates/precursors leading to AlPO crystallites. This analysis revealed that the Zn^{2+}-containing gel contained slightly larger particles (11.5 nm) than those seen in AlPO-5 crystallization which were observed to grow to ~12 nm before the onset of crystallization [determined through both the appearance of a number of reflections consistent with ZnAPO-34 as well as small changes in the first EXAFS oscillation and the presence of a multiple-scattering feature at 9.685 keV in the XANES (feature 'A' in Fig. 4(a)] at the comparatively low temperature of 369 K. The Avrami–Erofe'ev analysis of the ZnAPO-34 crystallization appears consistent with a phase-boundary-controlled three-dimensional growth process with a decreasing nucleation rate.

Interestingly the Avrami exponents obtained from profiling reflect the dimensionality of the final microporous material (Beale *et al.*, 2006). As with the crystallization of the AlPO-5 phase, the initial crystallite sizes were very similar to the size of the average aggregates seen in the gel immediately before the crystalline material began to form.

In Fig. 4 we show the raw XAFS, SAXS and WAXS data collected during the heating (at a rate of 1 K min^{-1} up to a temperature of 453 K) of the zinc-doped aluminophosphate gel.

The implication for the similarity of the average SAXS aggregate size to that of the first crystallite is that a type of gel reorganization precedes the formation of crystalline AlPO-5 and ZnAPO-34 phases. Further support for this notion can be found from a further analysis of the SAXS data. An initial observation that can be made here is that in the SAXS $I(q)$ *versus* q data there are only small changes visible. However, the most sensitive parameter to changes in the sample
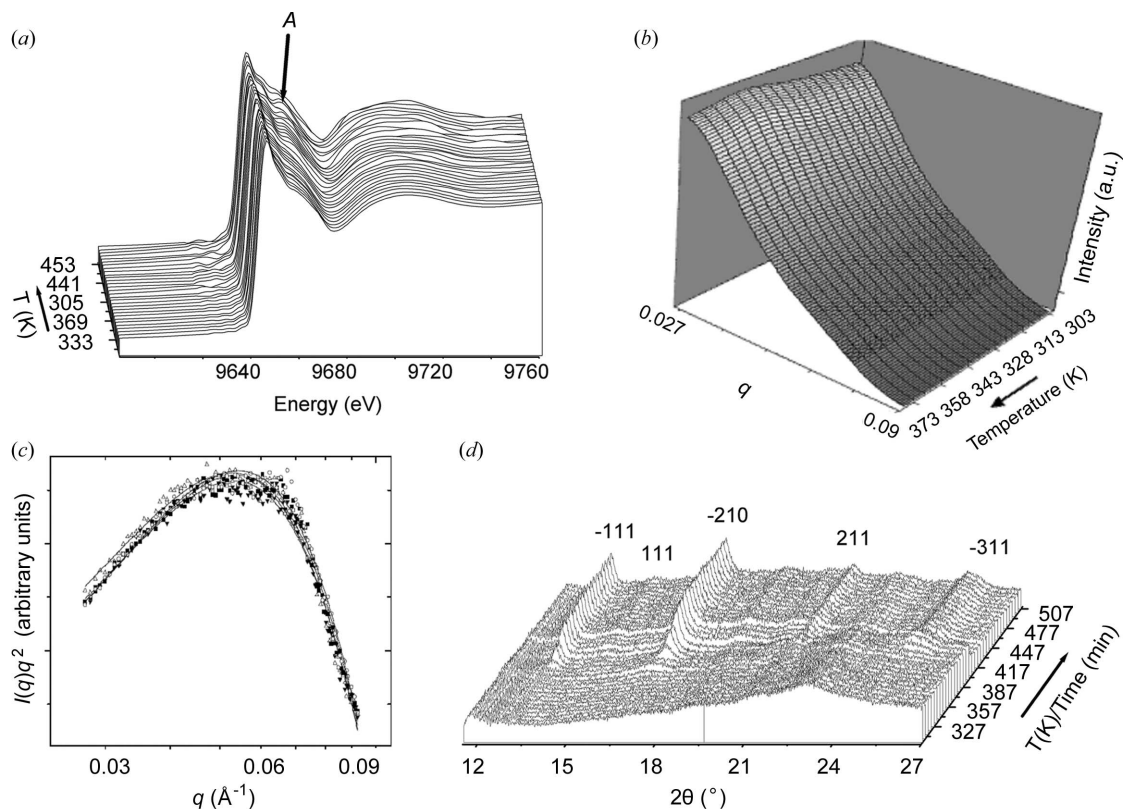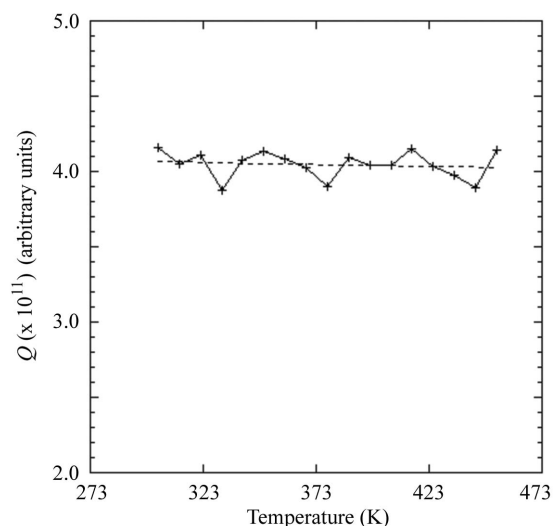
Figure 4
Combined *in situ* XANES (*a*), SAXS (*b*) [with accompanying Gaussian fits to the data (*c*)] and WAXS (*d*) data collected during the hydrothermal crystallization of ZnAlPO-34. Note that the additional oscillations observed in the pre-edge region of the XANES data are artefacts caused by sample movement. The feature highlighted *A* in (*a*) illustrates the appearance of a feature at 9.685 keV, appearing at the onset of crystallization. Although the variations in the SAXS data are not very large, the change in the shape of the curves is evident.

morphology is the invariant defined for a two-phase system by Porod (Porod, 1951),

$$Q = \int I(\mathbf{q}) \, dV = \int\limits_{q=0}^{q=\infty} I(q)q^2 \, dq = \langle n_e \rangle^2 \varphi_1 \varphi_2,$$

in which $\langle n_e \rangle^2$ is the electron density difference between two phases, and φ_i are the volume fractions for the two components. This equation can be generalized to a multi-component system (Goodisman & Brumberger, 1971). In Fig. 5 we plot the development of the invariant *versus* time during the crystallization process. The striking observation is that there is hardly any change in the invariant whilst the WAXS data clearly indicate that crystallization occurs on reaching ~369 K. It has been shown that the invariant is a more sensitive parameter to the occurrence of crystallization than the WAXS peak intensities are (Bras *et al.*, 2003). Therefore the lack of change in the invariant can be interpreted in two ways: either the change in electron density contrast between the two phases is offset by the changes in the respective volume fractions, or both the electron density contrast and the volume fractions remain unchanged. The latter option would entail that large amorphous domains are already present. The physical process that takes place during the crystallization is therefore a rearrangement of the components from an amor-

Figure 5
Development of the invariant as a function of temperature (time). The dashed line represents a linear fit to the data. The maximum deviation of the data to this linear fit is 4%. The variation of the linearly fitted data over this temperature range is about 1%.

phous state to a crystalline state. The surrounding matrix is not influenced by this, neither is the density of the newly formed crystalline state changed.
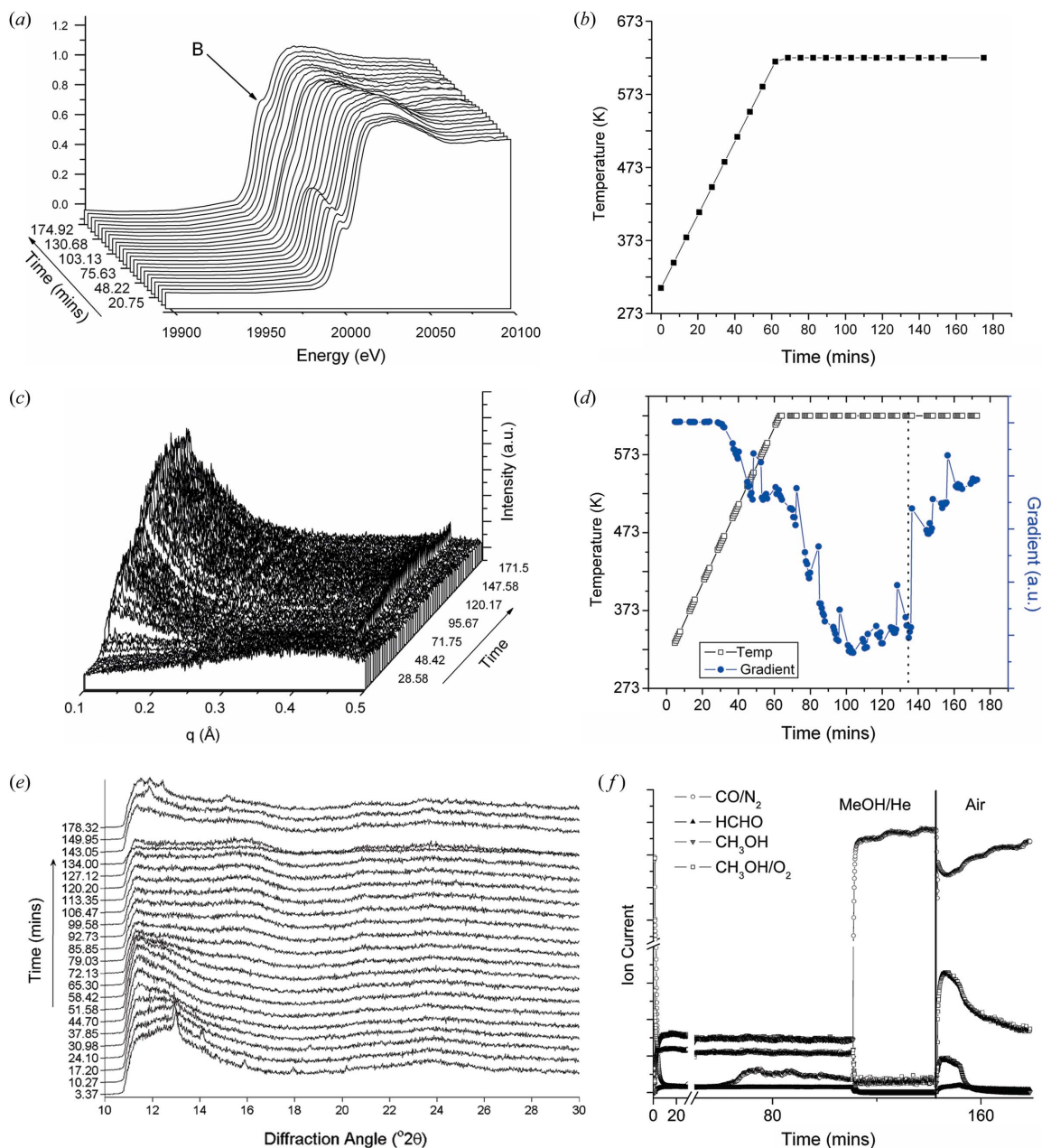
Figure 6
Combined Mo K-edge XANES (a) with combined temperature/time profile (b), raw SAXS data (c) with analysis of gradient *versus* time (d), WAXS (e) and mass spectrometry data (f) recorded during the heating of a FeMo catalyst under MeOH/He and in air conditions. Feature B in (a) highlights the 1s–4d peak at the Mo K-edge.

3.2. Catalytic investigation of the behaviour of iron molybdate catalyst for methanol dehydrogenation

As mentioned previously, combined SAXS/WAXS/XAFS experiments have also been performed to study heterogeneous catalytic reactions in the gas phase. As can be seen in Fig. 6, the initial starting 'FeMo' phase contained only a few weak reflections and a broad hump between 11 and 15° 2θ, but has been previously identified as possessing a structure similar to that of poorly crystalline Mo_5O_{14} (Beale *et al.*, 2008). However, as heating began, dramatic changes in all three techniques (SAXS/WAXS/XAFS) occurred, which suggested

that the initial 'FeMoO' phase was unstable up to a certain temperature. More specifically, the peaks and broad hump ascribable to the initial Mo_5O_{14}-type phase were observed to disappear with time resulting in an essentially featureless WAXS pattern as the temperature approached 623 K (~60 min). On switch over to air, in order to regenerate the catalyst, new Bragg reflections appeared in the X-ray diffraction pattern at ~11.70, 12.30, 15.15 and 23.40° 2θ which can be ascribed to the ($\bar{2}$14), ($\bar{4}$02), (122/$\bar{3}$22) and ($\bar{1}$16/420/204/$\bar{5}$16) reflections of $Fe_2(MoO_4)_3$ as well as a peak at 11.95° 2θ owing to the strongest reflection of β-$FeMoO_4$. At the same time the 1s–4d transition [marked B in Fig. 6(a)] at

20001.74 eV, which is known to be sensitive to both the oxidation and coordination state of Mo (Beale & Sankar, 2003), was observed to first decrease in intensity as the temperature approached 623 K ($\sim$60 min), before disappearing entirely after 130 min of reaction. Such changes would be consistent with the reduction of the initial octahedral $Mo^{5/6+}$ species to a lower oxidation state. On regeneration with air (after 130 min) the $1s$–$4d$ transition reappeared, although this time was much more intense and appeared at a slightly lower position in energy (20000.5 eV). Most likely the increased intensity of this feature originates from a 'pinhole' effect in the sample and subsequent detector saturation. In the SAXS data a feature at $q = 0.12$ Å was also observed to begin to form after $\sim$23–28 min of reaction (427–451 K) and continue to increase in intensity for a further 40 min. Such a feature would be consistent with the formation and growth (proposed from an analysis of the change in slope) of particulate species although it is not clear whether this was related to the phase changes observed in the WAXS or maybe the formation of something on the catalyst surface, e.g. coke. Interestingly, no evidence could be observed for the formation of formaldehyde ($m/z = 31$) from the mass spectrometer trace during reaction (Fig. 6f), although the catalyst proved active for CO production (and, although not shown here, H_2); initially in small(er) amounts as the temperature approached 623 K ($\sim$65 min) although later (after 110 min) in much larger quantities. The sudden increase in CO production after 110 min is difficult to explain, although it may be related to the formation of a particularly active reduced phase for methanol breakdown. Further studies and analysis of the data is in progress. In summary, from this initial study it is possible to propose that the initial Mo_5O_{14}-type phase undergoes a number of significant changes during heating in methanol, including both reduction and a phase change, eventually leading to a catalyst which is active for methanol breakdown. Such observations have important implications when determining the stability and activity of this catalyst under reaction conditions. However, it is worth emphasizing at this point that the instrumentation that has been developed is sufficiently versatile that not only X-ray-based data can be collected but also that the system is flexible enough to incorporate complicated sample environments as well as additional non-X-ray-based spectroscopic techniques.

4. Conclusions

The experiments carried out demonstrate the feasibility of a three-technique set-up to obtain in situ correlated data at the nanometre to micrometre scale, enabling new insight into materials' self-assembly and catalytic processes. Further geometrical and optical optimization is possible, which will result in improved SAXS/WAXS data quality, and the planned software development will result in better time resolution. These future developments will make the set-up suitable for performing experiments which show changes at the 20–30 s time scale. This sort of time resolution will mean that the set-up will be applicable for studying many chemical/physical processes in the chemical industries, but there are also many examples (e.g. formation of nanoparticles, polymers etc.) where more fundamental research can benefit from the availability of such experimental equipment. The equipment is unlikely to be applicable yet for the study of very fast processes (with subsecond changes). This obviously remains the preserve of energy-dispersive techniques or fast sequential energy-scanning EXAFS set-ups (Frahm et al., 2004). On the other hand, the method that we have developed has the big advantage that the instantaneous radiation dose received by the sample is much lower than compared with energy-dispersive techniques which means that the sample has a chance of surviving much longer.

References

Bark, M., Zachmann, H. G., Alamo, R. & Mandelkern, L. (1992). Makromol. Chem. **193**, 2363–2377.

Beale, A. M. & Sankar, G. (2003). Chem. Mater. **15**, 146–153.

Beale, A. M., van der Eerden, A. M. J., Jacques, S. D. M., Leynaud, O., O'Brien, M. G., Meneau, F., Nikitenko, S., Bras, W. & Weckhuysen, B. M. (2006). J. Am. Chem. Soc. **128**, 12386–12387.

Beale, A. M., van der Eerden, A. M. J., Kervinen, K., Newton, M. A. & Weckhuysen, B. M. (2005). Chem. Commun. pp. 3015–3017.

Beale, A. M. et al. (2008). In preparation.

Borsboom, M., Bras, W., Cerjak, I., Detollenaere, D., Glastra van Loon, D., Goedtkindt, P., Konijnenburg, M., Lassing, P., Levine, Y. K., Munneke, B., Oversluizen, M., van Tol, R. & Vlieg, E. (1998). J. Synchrotron Rad. **5**, 518–520.

Bras, W. (1998). J. Macromol. Sci. B**37**, 557–565.

Bras, W., Derbyshire, G. E., Bogg, D., Cooke, J., Elwell, M. J., Komanschek, B. U., Naylor, S. & Ryan, A. J. (1995). Science, **267**, 996–999.

Bras, W., Derbyshire, G. E., Devine, A., Clark, S. M., Cooke, J., Komanschek, B. E. & Ryan, A. J. (1995). J. Appl. Cryst. **28**, 26–32.

Bras, W., Derbyshire, G. E., Ryan, A. J., Mant, G. R., Felton, A., Lewis, R. A., Hall, C. J. & Greaves, G. N. (1993). Nucl. Instrum. Methods Phys. Res. A, **326**, 587–591.

Bras, W., Dolbnya, I. P., Detollenaere, D., van Tol, R., Malfois, M., Greaves, G. N., Ryan, A. J. & Heeley, E. (2003). J. Appl. Cryst. **36**, 791–794.

Bras, W., Greaves, G. N., Oversluizen, M., Clark, S. M. & Eeckhaut, G. (2005). J. Non-Cryst. Solids, **351**, 2178–2193.

Bras, W. & Ryan, A. J. (1998). Adv. Colloid Interface Sci. **75**, 1–43.

Briois, V., Lutzenkirchen-Hecht, D., Villain, F., Fonda, E., Belin, S., Griesebock, B. & Frahm, R. (2005). J. Phys. Chem. A**109**, 320–329.

Bryant, G. K., Gleeson, H. F., Ryan, A. J., Fairclough, J. P. A., Bogg, D., Goossens, J. G. P. & Bras, W. (1998). Rev. Sci. Instrum. **69**, 2114–2117.

Christensen, N., Jensen, T. R., Norby, P. & Hanson, J. C. (1998). Chem. Mater. **10**, 1688–1693.

research papers

Clausen, B. S., Steffensen, G., Fabius, B., Villadsen, J., Feidenhansl, R. & Topsoe, H. (1991). *J. Catal.* **132**, 524–535.

Derbyshire, G., Cheung, K.-C., Sangsingkeow, P. & Hasnain, S. S. (1999). *J. Synchrotron Rad.* **6**, 62–63.

Farrow, R., Derbyshire, G. E., Dobson, B. R., Dent, A. J., Bogg, D., Headspith, J., Lawton, R., Martini, M. & Buxton, K. (1995). *Nucl. Instrum. Methods Phys. Res. B*, **97**, 567–571.

Frahm, R. (1988). *Nucl. Instrum. Methods Phys. Res. A*, **270**, 578–581.

Frahm, R. (1989). *Rev. Sci. Instrum.* **60**, 2515–2518.

Frahm, R., Griesebock, B., Richwin, M. & Lützenkirchen-Hecht, D. (2004). *AIP Conf. Proc.* **705**, 1411–1415.

Gabriel, A. & Dauvergne, F. (1982). *Nucl. Instrum. Methods Phys. Res.* **201**, 223–224.

Goodisman, J. & Brumberger, H. (1971). *J. Appl. Cryst.* **4**, 347–351.

Grandjean, D., Beale, A. M., Petukhov, A. V. & Weckhuysen, B. M. (2005). *J. Am. Chem. Soc.* **127**, 14454–14465.

Hulbert, S. F. (1969). *J. Br. Ceram. Soc.* **6**, 11–20.

Mesu, J. G., van der Eerden, A. M. J., de Groot, F. M. F. & Weckhuysen, B. M. (2005). *J. Phys. Chem. B*, **109**, 4042–4047.

Newton, M. A., Jyoti, B., Dent, A. J., Fiddy, S. G. & Evans, J. (2004). *Chem. Commun.* pp. 2382–2383.

Porod, G. (1951). *Kolloid Z. Z. Polym.* **124**, 83–114.

Sankar, G., Thomas, J. M., Rey, F. & Greaves, G. N. (1995). *J. Chem. Soc. Chem. Commun.* pp. 2549–2550.

Sankar, G., Wright, P. A., Natarajan, S., Thomas, J. M., Greaves, G. N., Dent, A. J., Dobson, B. R., Ramsdale, C. A. & Jones, R. H. (1993). *J. Phys. Chem.* **97**, 9550–9554.

Savarino, L., Stea, S., Granchi, D., Donati, M. E., Cervellati, M., Moroni, A., Paganetto, G. & Pizzoferrato, A. (1998). *J. Mater. Sci.* **9**, 109–115.

Scheidegger, A. M., Wieland, E., Scheinost, A. C., Dahn, R. & Spieler, P. (2000). *Environ. Sci. Technol.* **34**, 4545–4548.

Scheidegger, A., Wieland, E., Scheinost, A. C., Dähn, R., Tits, J. & Spieler, P. (2001). *J. Synchrotron Rad.* **8**, 916–918.

Soares, A. P. V. & Portela, M. F. (2005). *Catal. Rev.* **47**, 125–174.

Weckhuysen, B. M., Baetens, D. & Schoonheydt, R. A. (2000). *Angew. Chem. Int. Ed.* **39**, 3419–3422.

Zachmann, H. G. & Wutz, C. (1993). *Crystallization of Polymers.* Dordrecht: Kluwer.